Anisotropic magnetoresistance and nontrivial spin Hall magnetoresistance in Pt/α-Fe_{2}O_{3} bilayers

Yang Cheng, Sisheng Yu, Adam S. Ahmed, Menglin Zhu, You Rao, Maryam Ghazisaeidi, Jinwoo Hwang, and Fengyuan Yang

Phys. Rev. B **100**, 220408 — Published 16 December 2019

DOI: 10.1103/PhysRevB.100.220408

Anisotropic Magnetoresistance and Nontrivial Spin Hall Magnetoresistance in Pt/α-Fe_2O_3 Bilayers

Yang Cheng[1,*], Sisheng Yu[1,*], Adam S. Ahmed[1], Menglin Zhu[2], You Rao,[2] Maryam Ghazisaeidi,[2] Jinwoo Hwang[2], Fengyuan Yang[1]

[1]Department of Physics, The Ohio State University, Columbus, OH, USA

[2]Department of Materials Science and Engineering, The Ohio State University, Columbus, OH, 43212, USA

[*]These two authors contributed equally to this work.

Abstract

Magnetic proximity effect has only been conclusively observed in ferromagnet-based systems. We report the observation of anomalous Hall effect and angular-dependent anisotropic magnetoresistance in Pt on antiferromagnetic α-Fe_2O_3(0001) epitaxial films at 10 K, which provide evidence for the magnetic proximity effect. The Néel order of α-Fe_2O_3 and the induced magnetization in Pt show a unique angular dependent magnetoresistance compared with all other ferromagnetic and antiferromagnetic systems. A macrospin response model is established and can explain the antiferromagnetic spin configuration and all main magnetoresistance features in the Pt/α-Fe_2O_3 bilayers.

Introduction. Antiferromagnets (AF) have recently generated significant excitements in spintronics due to their terahertz response, high speed, low energy cost, and abundance of materials [1-17]. Magnetic proximity effect (MPE) is an important phenomenon in spintronics with great potential for application, such as spin logic devices, modulating spin currents in graphene, and realizing high temperature quantum anomalous Hall effect in topological insulators [17-26].

To date, MPE has only been conclusively observed in nonmagnetic heavy metals (HM) on ferromagnets (FMs) [17-26]. An intriguing question is whether MPE exists in HM/AF systems. In principle, because MPE in HM/FMs originates from the surface magnetic moments, AFs with uncompensated surface moment should also be able to induce MPE. Kosub, *et al.* [27] reported that MPE might exist in Pt/Cr_2O_3 bilayers evidenced by the anomalous Hall effect (AHE), which is not conclusive (see *Supplementary Materials* [28] and references [29-48] therein). We report the evidence of MPE in Pt/α-Fe_2O_3 bilayers which exhibit both the AHE and anisotropic magnetoresistance (AMR). We explain our data by modeling the Néel order in α-Fe_2O_3 and MPE-induced moment in Pt, and the competition between the spin-flop transition and the anisotropies in α-Fe_2O_3.

Experimental Results. Epitaxial α-Fe_2O_3(30 nm) films are grown on Al_2O_3(0001) substrates using off-axis sputtering [49-51] at a substrate temperature of 500°C, followed by the in-situ deposition of a 2-nm Pt layer on α-Fe_2O_3 at room temperature. The quality of the films is first examined by X-ray diffraction (XRD). Figure 1(a) shows a $2\theta/\omega$ XRD scan for a Pt(2 nm)/α-Fe_2O_3(30 nm) bilayer, where the clear Laue oscillations (right inset) and narrow rocking curve with a full-width-at-half-maximum (FWHM) of 0.043° (left insert) indicate high crystalline quality. X-ray reflectometry scan (see *Supplementary Materials* [28]) for the 30-nm α-Fe_2O_3

film gives a roughness of 0.2 nm. The smooth surface of the α-Fe_2O_3 film is confirmed by atomic force microscopy (AFM) as shown in Fig. 1(b), which gives a roughness of 0.1 nm. Figures 1(c) and 1(d) show cross-sectional scanning transmission electron microscopy (STEM) images of the α-Fe_2O_3/Al_2O_3 and Pt/α-Fe_2O_3 interfaces, respectively, which reveal clean interfaces.

The Pt(2 nm)/α-Fe_2O_3(30 nm) bilayer is patterned into a 100 μm wide Hall bar. Figure 2(a) shows the Hall loops at 10 and 100 K in an out-of-plane field $\boldsymbol{H}$. Hall resistance (R_{xy}) generally includes the ordinary Hall effect (OHE) and anomalous Hall effect (AHE). The OHE is linearly proportional to H while the AHE is typically seen in FMs and proportional to its out-of-plane magnetization [52]. In Fig. 2(a), a clear AHE signal emerges at 10 K, but disappears at 100 K.

To probe the origin of the observed AHE at 10 K and the spin configuration in α-Fe_2O_3, we measure the angular dependent magnetoresistance (ADMR) $\Delta\rho_{xx}/\rho_0$ for the Pt(2 nm)/α-Fe_2O_3(30 nm) bilayer, where ρ_0 is the longitudinal resistivity at zero field. Figure 2(b) shows the schematics of the Hall bar with angle α, β, and γ defined between $\boldsymbol{H}$ and the x, z, and z axes in the xy, yz, and zx planes, respectively, where the current **I** is along the x-axis. Figure 2(c) shows the γ-scan magnetoresistance (MR) at 10 K, where a sharp peak is observed when $\boldsymbol{H} \perp$ film (γ = 0° and 180°) at $\mu_0 H$ = 1-14 T. The peak becomes narrower as H increases, while the peak magnitude remains essentially the same. In Fig. 2(c), at $\mu_0 H \geq 7$ T, the MR exhibits local maxima at γ = 90° and 270°, which is a signature for the AMR [53-56]. The AMR saturates with a magnitude of ~0.01% at 7 T, which is consistent with the Hall loop at 10 K in Fig. 2(a). To explore its temperature dependence, we measure the γ-scans at 14 T for the sample at 10 and 300 K, which display opposite angular dependencies as shown in Fig. 2(d) (ignore the sharp peaks for now).

We next make two control samples (more discussions in the section below), a 2 nm Pt layer and a Pt(8 nm)/α-Fe_2O_3(30 nm) bilayer on Al_2O_3(0001) for the same measurement at 10 K, as shown in Figs. 2(e) and 2(f). Both samples have $\sin\gamma^2$ dependence, as expected from the ordinary magnetoresistance (OMR). The OMR in Pt(2 nm)/Al_2O_3 is understood. The Pt(8 nm)/α-Fe_2O_3 result will be discussed in the next section. Another interesting feature is that the sharp peak near γ =180° observed in the Pt(2 nm)/α-Fe_2O_3 bilayer also appears in the Pt(8 nm)/α-Fe_2O_3, which cannot be explained by AMR. Below we use β- and α-scan MR to uncover its mechanism.

Figure 3(a) shows the β-scans for the Pt/α-Fe_2O_3 bilayer at 10 K. Sharp peaks are also observed near β = 0° and 180°, but opposite to those in the γ-scans. At $\mu_0 H$ = 1 T, the β-scan has local maxima at β = 90° and 270° with a magnitude of ~0.01%, which has been reported before in YIG/NiO/Pt [57, 58] and attributed to the Néel order $\boldsymbol{n} \perp \boldsymbol{H}$. Consequently, the β-scans show a negative spin Hall magnetoresistance (SMR) that has a 90° phase shift compared with the positive SMR in Pt/FM bilayers. As H increases, the β-scans become flat and eventually have local minima at β = 90° and 270° at 14 T due to the dominant OMR over the negative SMR at high fields. By comparing the 14-T β-scans at 10 and 300 K in Fig. 3(b) and the OMR-only 14-T β-scan of Pt(2 nm)/Al_2O_3 at 10 K in Fig. 3(c), it is clear that the β-scans in Fig. 3(a) are due to the competition between the OMR that dominates at high fields, and the negative SMR that dominates at low fields.

Figure 3(d) shows the α-scans for the Pt/α-Fe_2O_3 bilayer at 10 K, which exhibit three notable features. First, no sharp peak is observed, but the magnitude of ADMR of ~0.1% is comparable to that of the sharp peaks in the β- and γ-scans. Second, at $\mu_0 H \geq 0.3$ T, the α-scans remain unchanged and can be well fit by $\sin^2\alpha$ with maxima at α = 90° and 270°, which is a

signature of negative SMR, indicating that $\boldsymbol{n}$ is perpendicular to the in-plane field due to the spin-flop transition. Third, for a small field of 0.1 T, the α-scan deviates from $\sin^2\alpha$, suggesting that $\boldsymbol{n}$ is in a multi-domain state (below the spin-flop field). Such a small spin-flop field of <0.3 T in epitaxial α-Fe_2O_3 films is 20× smaller than the ~6 T in bulk α-Fe_2O_3 [59].

Figure 3(e) shows two α-scans at 14 T, where the MR at 300 K is 50% larger than that at 10 K. As a comparison, the OMR in a Pt(2 nm)/Al_2O_3 control sample exhibits no α-dependence [Fig. 3(f)]. The 300 K α-scan in Fig. 3(e) is due to pure SMR while the 10 K data is dominated by SMR, but with an opposite contribution from AMR. This is because SMR has a weak temperature dependence and AMR vanishes at 300 K. For the SMR, $\Delta\rho_{xx}/\rho_0 = \theta_{\mathrm{SH}}^2\frac{\lambda}{d}(2\lambda G\tanh^2\frac{d}{2\lambda})/(\frac{1}{\rho}+2\lambda G\coth\frac{d}{\lambda})$, where G, θ_{SH}, λ, d, ρ are the spin mixing conductance, spin Hall angle, spin diffusion length, thickness, and resistivity of Pt, respectively [60, 61]. Using $\Delta\rho_{xx}/\rho_0 = 0.15\%$ at 300 K and 14 T in the α-scans, $\theta_{\mathrm{SH}} = 0.086$, λ = 1.2 nm [62], d = 2 nm, and $\rho = 2.5 \times 10^{-7}$ Ω·m, we obtain $G = 5.5 \times 10^{15}$ $\Omega^{-1}\cdot m^{-2}$, which is an order of magnitude higher than other AFs [17, 63, 64].

Discussion. In this section, we provide likely explanations for our experimental results. First, the Hall loops at 10 and 100 K shown in Fig. 2(a) suggest that our AHE signal likely arises from the MPE-induced magnetization in Pt due to the interfacial exchange interaction, which is suppressed by thermal fluctuations at higher temperatures [53, 54]. An alternative origin is the spin-Hall-induced AHE in Pt/α-Fe_2O_3 [60]. However, in that case, the AHE should survive even at 300 K because of the weak temperature dependence of the spin Hall effect and the high Néel temperature (T_N = 955 K) of α-Fe_2O_3 [65]. Second, previous studies of Pt/FM bilayers show that the existence of AMR can be used to probe the MPE. From our ADMR measurements on Pt/α-Fe_2O_3, AMR is observed in the γ-scan at 10 K with a saturation magnitude of ~0.01% as shown

in Fig. 2(c), which is close to the MPE-induced AMR in Pt/$CoFe_2O_4$ [53]. In addition, Fig. 2(d) shows the opposite angular dependencies (excluding the sharp peaks) of MR between 10 and 300 K, indicating that the OMR, which has the same physical origin as OHE and has an opposite angular dependence to AMR, should dominate at 300 K. The disappearance of AMR at 300 K is expected if the AMR is induced by the MPE which is known to decrease at higher temperatures, consistent with the Hall data. Third, in our control measurements shown in Figs. 2(e) and 2(f), the Pt(8 nm)/α-Fe_2O_3 bilayer exhibits no AMR signal. This rules out the possibility that the Pt magnetization is due to the formation of magnetic FePt alloy by interdiffusion, demonstrating that the induced magnetization in Pt is an interfacial effect. For the Pt(8 nm)/α-Fe_2O_3, the AMR is overwhelmed by the OMR in Pt, while for the Pt(2 nm)/α-Fe_2O_3, the AMR dominates OMR. Thus, the AMR in Pt(2 nm)/α-Fe_2O_3 is likely due to the MPE-induced magnetization in Pt.

To explain the SMR features in the α-, γ-, and β-scans, we use a macrospin response model (see *Supplementary Materials* [28]) to describe the AF spins based on the free energy [66, 67],

$$E(\boldsymbol{n}) = H_{k1}(\boldsymbol{n}\cdot\hat{\boldsymbol{z}})^2 + H_{k2}\cos[6(\varphi_N-\delta)] + \frac{H^2}{2H_e}(\boldsymbol{h}\cdot\boldsymbol{n})^2, \quad (1)$$

where $\boldsymbol{n}$ is the unit vector of Néel order, φ_N is the in-plane angle between $\boldsymbol{n}$ and the x-axis, and δ is the phase angle that defines the orientations of the easy axes. H_{k1} and H_{k2} are the easy-plane and in-plane easy-axis anisotropy, respectively, both of which are positive, indicating in-plane Néel order with three easy-axes that are 60° apart. $\boldsymbol{h}$ is the unit vector of the applied field and H_e is the exchange field between the AF spins. The last term corresponds to the AF spin-flop transition, which prefers $\boldsymbol{h}\perp\boldsymbol{n}$. By minimizing $E(\boldsymbol{n})$, we extract the Néel order in response to $\boldsymbol{H}$.

Figure 4(a) shows the schematics of $\boldsymbol{n}$ in three regimes: $\theta_H \sim 90°$, $\theta_H = 0°$, and in

between, where θ_{H} is the angle between $\boldsymbol{H}$ and the z-axis, $\mathbf{I} \parallel x$-axis, and $\boldsymbol{H}$ lies in the yz-plane. Due to the strong easy-plane anisotropy H_{k1}, $\boldsymbol{n}$ always stays in-plane. The competition between H_{k2} and the spin-flop term determines φ_N. The three kinds of MR are then given by [17, 53],

$$\begin{aligned} &\rho_{xx}^{\mathrm{AMR}} \propto (m_x^{\mathrm{Pt}})^2 \propto h_x^2 \propto \sin^2\theta_{\mathrm{H}}, \\ &\rho_{xx}^{\mathrm{SMR}} \propto -n_y^2 = -(1-n_x^2) \propto -\sin^2\varphi_N, \\ &\rho_{xx}^{\mathrm{OMR}} \propto -h_x^2 \propto -\sin^2\theta_{\mathrm{H}}, (\boldsymbol{H} \text{ in either the } yz\text{- or the } zx\text{-plane}) \end{aligned} \tag{2}$$

where ρ_{xx}^{AMR} is assumed to be induced by the magnetization in Pt. To fit the MR data, we choose $H_{k1} = 2$ T, $H_{k2} = 2$ G, $H_e = 50$ T, and $\delta = -2.5°$ (a small non-zero δ to lift degeneracy) to first obtain the θ_{H}-dependence of φ_N, as shown in Fig. 4(b). As θ_{H} is close to 90° [left, Fig. 4(a)], φ_N approaches 0°, indicating that the spin-flop term dominates and $\boldsymbol{n} \perp \boldsymbol{H}$. As θ_{H} rotates toward 0° [middle, Fig. 4(a)], the spin-flop term decreases and $\boldsymbol{n}$ rotates towards one of the three easy-axes. For small field like 1 T, the rotation of $\boldsymbol{n}$ is gradual. For $\mu_0 H \geq 10$ T, the in-plane component of $\boldsymbol{H}$ at $\theta_H \geq 5°$ is large enough to align $\boldsymbol{n}$ along the x-axis (φ_N = 0°), and at $\theta_{\mathrm{H}} < 5°$, φ_N increases dramatically. At $\theta_{\mathrm{H}} = 0°$ [right, Fig. 4(a)], the spin-flop term is 0 and $\boldsymbol{n}$ has equal probability to align along any of the three easy axes, forming multi-domains.

This mechanism can simultaneously explain the sharp peaks in the γ- and β-scans, the small negative SMR in the β-scans, and the large negative SMR in the α-scans. For the γ-scans away from 0° or 180°, the in-plane component of $\boldsymbol{H}$ is large enough to induce the spin-flop transition and the α-Fe_2O_3 film is a single domain with $\boldsymbol{n} \parallel y$-axis. As γ approaches 0° or 180°, the in-plane component of $\boldsymbol{H}$ drops below the spin-flop field and the α-Fe_2O_3 film forms multi-domains with a significant n_x, resulting in a sharp increase in the SMR. Meanwhile, in the β-scans, as β approaches 0° or 180°, the α-Fe_2O_3 film enters the multi-domain regime and $\boldsymbol{n}$ rotates away from the x-axis, resulting in a sudden decrease in SMR. The peaks are sharper at higher

fields because of the constant in-plane spin-flop field and sharper change of φ_N [see Fig. 4(b)]

In Fig. 3(d), at $\mu_0 H = 0.1$ T, the α-scan deviates from $\sin^2\alpha$, indicating the AF is in multi-domains. An in-plane $\mu_0 H \geq 0.3$ T overcomes H_{k2} and induces the spin-flop transition to form a single domain, which corresponds to 1.2° off the z-axis at 14 T. The magnitude of AMR in the α-scans is similar to that in the γ-scans, which is ~10× smaller than the SMR with opposite angular dependence. Using $H_{k1} = 2$ T, $H_{k2} = 2$ G, $H_e = 50$ T, and $\delta = -2.5°$, we show the fitting of the γ- and β-scans in Figs. 4(c) and 4(d), respectively. The fitting reproduces all the key features discussed above, including the whole angular and field range of the ADMR scans.

To further understand the implied MPE in the Pt/α-Fe_2O_3 bilayers, we use density functional theory (DFT) to calculate the induced magnetization in Pt on Fe_2O_3 assuming an atomic flat (0001) surface with ferromagnetically aligned AF spins (see Supplementary Materials for more DFT results and discussion). Figure 5 shows the average magnetic moments of Pt in the vicinity of the interface. The magnitude of the magnetic moment starts at over 0.16 μ_B/atom in the first two Pt layers and decreases at layer 3 away from the interface. In layer 4 and layer 5, the magnetic moments approach zero with minor fluctuations, suggesting that the presence of the Pt moments comes from the magnetism induced by Fe_2O_3.

Conclusion. Our experimental results provide evidence for MPE in the Pt/α-Fe_2O_3 bilayers, which most likely arises from the uncompensated surface spins of α-Fe_2O_3 [27, 68]. In our model, we assume that the AMR is induced by the MPE and the MPE-induced magnetization in Pt is parallel to ***H***, which fits our experimental data well. We note that our results cannot rule out other possible mechanisms for MPE, such as local ferromagnetism induced by nonuniformities or defects at the interface. The confirmation of the MPE needs more direct measurement of the induced moment in Pt on Fe_2O_3, such as using X-ray magnetic circular dichroism (XMCD). The

interpretation of the AF-induced MPE requires a more rigorous theoretical understanding of the surface AF spin structure on Fe_2O_3.

This work was supported primarily the U.S. Department of Energy (DOE) under Grant No. DE-SC0001304 (YC, SSY, and FYY), and partially supported by the Center for Emergent Materials, an NSF MRSEC, under Grant No. DMR-1420451 (ASA, MLZ, and JH).

Figure Captions:

Figure 1. (a) XRD $2\theta/\omega$ scan of a Pt(2 nm)/α-Fe_2O_3(30 nm) bilayer on Al_2O_3(0001). Right inset: high-resolution scan of the α-Fe_2O_3 (0006) peak with Laue oscillations. Left inset: XRD rocking curve of the α-Fe_2O_3 (0006) peak. (b) AFM image of an α-Fe_2O_3(30 nm) with a roughness of 0.1 nm. STEM images of the (c) α-Fe_2O_3/Al_2O_3 and (d) Pt/α-Fe_2O_3 interfaces viewed along $(1\bar{2}10)$ and $(5\bar{4}10)$, respectively.

Figure 2. (a) Hall resistance for a Pt(2 nm)/α-Fe_2O_3(30 nm) bilayer at 10 and 100 K. (b) Schematics of α (*xy*-plane), γ (*zx*-plane), and β (*yz*-plane) angular dependence measurements. (c) γ-scans of a Pt(2 nm)/α-Fe_2O_3(30 nm) sample at 10 K an various magnetic fields, which show a sharp peak at out-of-plane field (0°, and 180°) and a broad peak at in-plane field (90° and 270°). Curves are shifted vertically for clarity. (d) γ-scans at 10 and 300 K for Pt(2 nm)/α-Fe_2O_3(30 nm) at 14 T. Control experiments of γ-scans for (e) a Pt(8 nm)/α-Fe_2O_3(30nm) bilayer and (f) a Pt(2 nm) on Al_2O_3(0001) taken at 14 T and 10 K, where OMR dominates the angular dependence. The red curves in (e) and (f) are cosine fits.

Figure 3. (a) β-scans of a Pt(2 nm)/α-Fe_2O_3(30 nm) bilayer at 10 K and various fields. (b) Comparison of the β-scans between 10 and 300 K at 14 T. (c) β-scan of a control sample Pt(2 nm) on Al_2O_3(0001) at 14 T and 10 K. (d) α-scans of a Pt(2 nm)/α-Fe_2O_3(30 nm) bilayer at 10 K and various fields. (e) Comparison of the α-scans between 10 and 300 K at 14 T. The solid curves in (c), (d), and (e) are cosine fits. (f) α-scan of a control sample Pt(2 nm) on Al_2O_3 (0001) at 14 T and 10 K. Curves are shifted vertically for clarity.

Figure 4. (a) Schematics of AF spin configurations as an applied field rotates from in-plane towards out-of-plane in the *yz*-plane (for β scans), where the green lines illustrate the three in-

plane easy axes of α-Fe_2O_3. (b) Simulation of φ_N, the angle between the Néel order $\boldsymbol{n}$ and the x-axis, at different field angle θ_H. Fitting of (c) γ-scans and (d) β-scans at 10 K for various fields, where the solid curves are fits to the experimental data. Curves are shifted vertically for clarity.

Figure 5. DFT calculations of the average magnetic moments for Pt atoms as a function of layer number away from the Pt/α-Fe_2O_3 interface. Error bars are the standard errors of the mean.

References:

1. W. Zhang, M. B. Jungfleisch, W. J. Jiang, J. E. Pearson, A. Hoffmann, F. Freimuth and Y. Mokrousov, "Spin Hall Effects in Metallic Antiferromagnets," *Phys. Rev. Lett.* **113**, 196602 (2014).
2. T. Jungwirth, X. Marti, P. Wadley and J. Wunderlich, "Antiferromagnetic spintronics," *Nat. Nanotechnol.* **11**, 231 (2016).
3. P. Wadley, B. Howells, J. Zelezny, C. Andrews, V. Hills, R. P. Campion, V. Novak, K. Olejnik, F. Maccherozzi, S. S. Dhesi, S. Y. Martin, T. Wagner, J. Wunderlich, F. Freimuth, Y. Mokrousov, J. Kunes, J. S. Chauhan, M. J. Grzybowski, A. W. Rushforth, K. W. Edmonds, B. L. Gallagher and T. Jungwirth, "Electrical switching of an antiferromagnet," *Science* **351**, 587 (2016).
4. A. H. MacDonald and M. Tsoi, "Antiferromagnetic metal spintronics," *Phil. Trans. Roy. Soc. A-Math. Phys. Eng. Sci.* **369**, 3098 (2011).
5. S. Urazhdin and N. Anthony, "Effect of polarized current on the magnetic state of an antiferromagnet," *Phys. Rev. Lett.* **99**, 046602 (2007).
6. R. Cheng, J. Xiao, Q. Niu and A. Brataas, "Spin Pumping and Spin-Transfer Torques in Antiferromagnets," *Phys. Rev. Lett.* **113**, 057601 (2014).
7. X. Marti, I. Fina, C. Frontera, J. Liu, P. Wadley, Q. He, R. J. Paull, J. D. Clarkson, J. Kudrnovsky, I. Turek, J. Kunes, D. Yi, J. H. Chu, C. T. Nelson, L. You, E. Arenholz, S. Salahuddin, J. Fontcuberta, T. Jungwirth and R. Ramesh, "Room-temperature antiferromagnetic memory resistor," *Nat. Mater.* **13**, 367 (2014).
8. S. Nakatsuji, N. Kiyohara and T. Higo, "Large anomalous Hall effect in a non-collinear antiferromagnet at room temperature," *Nature* **527**, 212 (2015).
9. H. L. Wang, C. H. Du, P. C. Hammel and F. Y. Yang, "Antiferromagnonic Spin Transport from $Y_3Fe_5O_{12}$ into NiO," *Phys. Rev. Lett.* **113**, 097202 (2014).
10. T. Satoh, R. Iida, T. Higuchi, M. Fiebig and T. Shimura, "Writing and reading of an arbitrary optical polarization state in an antiferromagnet," *Nat. Photonics* **9**, 25 (2015).
11. H. L. Wang, C. H. Du, P. C. Hammel and F. Y. Yang, "Spin transport in antiferromagnetic insulators mediated by magnetic correlations," *Phys. Rev. B* **91**, 220410(R) (2015).
12. R. Cheng, D. Xiao and A. Brataas, "Terahertz Antiferromagnetic Spin Hall Nano-Oscillator," *Phys. Rev. Lett.* **116**, 207603 (2016).
13. A. Prakash, J. Brangham, F. Y. Yang and J. P. Heremans, "Spin Seebeck effect through antiferromagnetic NiO," *Phys. Rev. B* **94**, 014427 (2016).
14. T. Kampfrath, A. Sell, G. Klatt, A. Pashkin, S. Mahrlein, T. Dekorsy, M. Wolf, M. Fiebig, A. Leitenstorfer and R. Huber, "Coherent terahertz control of antiferromagnetic spin waves," *Nat. Photonics* **5**, 31 (2011).
15. S. Seki, T. Ideue, M. Kubota, Y. Kozuka, R. Takagi, M. Nakamura, Y. Kaneko, M. Kawasaki and Y. Tokura, "Thermal Generation of Spin Current in an Antiferromagnet," *Phys. Rev. Lett.* **115**, 266601 (2015).
16. X. Z. Chen, R. Zarzuela, J. Zhang, C. Song, X. F. Zhou, G. Y. Shi, F. Li, H. A. Zhou, W. J. Jiang, F. Pan and Y. Tserkovnyak, "Antidamping-Torque-Induced Switching in Biaxial Antiferromagnetic Insulators," *Phys. Rev. Lett.* **120**, 207204 (2018).
17. L. Baldrati, A. Ross, T. Niizeki, C. Schneider, R. Ramos, J. Cramer, O. Gomonay, M. Filianina, T. Savchenko, D. Heinze, A. Kleibert, E. Saitoh, J. Sinova and M. Klaui, "Full angular dependence of the spin Hall and ordinary magnetoresistance in epitaxial antiferromagnetic NiO(001)/Pt thin films," *Phys. Rev. B* **98**, 024422 (2018).
18. Z. L. Jiang, C. Z. Chang, C. Tang, P. Wei, J. S. Moodera and J. Shi, "Independent Tuning of

Electronic Properties and Induced Ferromagnetism in Topological Insulators with Heterostructure Approach," *Nano Letters* **15**, 5835 (2015).
19. I. Vobornik, U. Manju, J. Fujii, F. Borgatti, P. Torelli, D. Krizmancic, Y. S. Hor, R. J. Cava and G. Panaccione, "Magnetic Proximity Effect as a Pathway to Spintronic Applications of Topological Insulators," *Nano Letters* **11**, 4079 (2011).
20. S. Y. Huang, X. Fan, D. Qu, Y. P. Chen, W. G. Wang, J. Wu, T. Y. Chen, J. Q. Xiao and C. L. Chien, "Transport Magnetic Proximity Effects in Platinum," *Phys. Rev. Lett.* **109**, 107204 (2012).
21. H. Nakayama, M. Althammer, Y. T. Chen, K. Uchida, Y. Kajiwara, D. Kikuchi, T. Ohtani, S. Geprags, M. Opel, S. Takahashi, R. Gross, G. E. W. Bauer, S. T. B. Goennenwein and E. Saitoh, "Spin Hall Magnetoresistance Induced by a Nonequilibrium Proximity Effect," *Phys. Rev. Lett.* **110**, 206601 (2013).
22. M. D. Li, C. Z. Chang, B. J. Kirby, M. E. Jamer, W. P. Cui, L. J. Wu, P. Wei, Y. M. Zhu, D. Heiman, J. Li and J. S. Moodera, "Proximity-Driven Enhanced Magnetic Order at Ferromagnetic-Insulator-Magnetic-Topological-Insulator Interface," *Phys. Rev. Lett.* **115**, 087201 (2015).
23. Z. Wang, C. Tang, R. Sachs, Y. Barlas and J. Shi, "Proximity-Induced Ferromagnetism in Graphene Revealed by the Anomalous Hall Effect," *Phys. Rev. Lett.* **114**, 016603 (2015).
24. F. Katmis, V. Lauter, F. S. Nogueira, B. A. Assaf, M. E. Jamer, P. Wei, B. Satpati, J. W. Freeland, I. Eremin, D. Heiman, P. Jarillo-Herrero and J. S. Moodera, "A high-temperature ferromagnetic topological insulating phase by proximity coupling," *Nature* **533**, 513 (2016).
25. F. Hellman, A. Hoffmann, Y. Tserkovnyak, G. S. D. Beach, E. E. Fullerton, C. Leighton, A. H. MacDonald, D. C. Ralph, D. A. Arena, H. A. Durr, P. Fischer, J. Grollier, J. P. Heremans, T. Jungwirth, A. V. Kimel, B. Koopmans, I. N. Krivorotov, S. J. May, A. K. Petford-Long, J. M. Rondinelli, N. Samarth, I. K. Schuller, A. N. Slavin, M. D. Stiles, O. Tchernyshyov, A. Thiaville and B. L. Zink, "Interface-induced phenomena in magnetism," *Rev. Mod. Phys.* **89**, 025006 (2017).
26. S. Singh, J. Katoch, T. C. Zhu, K. Y. Meng, T. Y. Liu, J. T. Brangham, F. Y. Yang, M. E. Flatte and R. K. Kawakami, "Strong Modulation of Spin Currents in Bilayer Graphene by Static and Fluctuating Proximity Exchange Fields," *Phys. Rev. Lett.* **118**, 187201 (2017).
27. T. Kosub, M. Kopte, F. Radu, O. G. Schmidt and D. Makarov, "All-Electric Access to the Magnetic-Field-Invariant Magnetization of Antiferromagnets," *Phys. Rev. Lett.* **115**, 097201 (2015).
28. See Supplemental Material at [URL] for addition results of XRD, SQUID, AFM, macrospin response model, AHE in Pt/AFI bilayers, control measurement of a Au/Fe_2O_3 bilayer, and DFT calculations.
29. A. N. Bogdanov, A. V. Zhuravlev and U. K. Rößler, "Spin-flop transition in uniaxial antiferromagnets: Magnetic phases, reorientation effects, and multidomain states," *Phys. Rev. B* **75**, 094425 (2007).
30. F. L. A. Machado, P. R. T. Ribeiro, J. Holanda, R. L. Rodríguez-Suárez, A. Azevedo and S. M. Rezende, "Spin-flop transition in the easy-plane antiferromagnet nickel oxide," *Phys. Rev. B* **95**, 104418 (2017).
31. L. J. De Jongh and A. R. Miedema, "Experiments on simple magnetic model systems," *Adv. Phys.* **50**, 947 (2001).
32. T. Kosub, S. Vélez, J. M. Gomez-Perez, L. E. Hueso, J. Fassbender, F. Casanova and D. Makarov, "Anomalous Hall-like transverse magnetoresistance in Au thin films on $Y_3Fe_5O_{12}$,"

Appl. Phys. Lett. **113**, 222409 (2018).
33. G. Kresse and J. Furthmüller, "Efficient iterative schemes for ab initio total-energy calculations using a plane-wave basis set," *Phys. Rev. B* **54**, 11169 (1996).
34. G. Kresse and D. Joubert, "From ultrasoft pseudopotentials to the projector augmented-wave method," *Phys. Rev. B* **59**, 1758 (1999).
35. S. L. Dudarev, G. A. Botton, S. Y. Savrasov, C. J. Humphreys and A. P. Sutton, "Electron-energy-loss spectra and the structural stability of nickel oxide: An LSDA+U study," *Phys. Rev. B* **57**, 1505 (1998).
36. J.-J. Tang and B. Liu, "Reactivity of the Fe_2O_3(0001) Surface for Methane Oxidation: A GGA + U Study," *J. Phys. Chem. C* **120**, 6642 (2016).
37. J. P. Perdew, K. Burke and M. Ernzerhof, "Generalized Gradient Approximation Made Simple," *Phys. Rev. Lett.* **77**, 3865 (1996).
38. D. C. Langreth and M. J. Mehl, "Beyond the local-density approximation in calculations of ground-state electronic properties," *Phys. Rev. B* **28**, 1809 (1983).
39. H. J. Monkhorst and J. D. Pack, "Special points for Brillouin-zone integrations," *Phys. Rev. B* **13**, 5188 (1976).
40. B. C. Bolding and E. A. Carter, "Minimization of Periodic-Boundary-Induced Strain in Interface Simulations," *Mol. Simulat.* **9**, 269 (1992).
41. L. I. Bendavid and E. A. Carter, "First principles study of bonding, adhesion, and electronic structure at the Cu_2O(111)/ZnO(10-10) interface," *Surf. Sci.* **618**, 62 (2013).
42. A. Kiejna and T. Pabisiak, "Surface properties of clean and Au or Pd covered hematite (α-Fe_2O_3) (0001)," *J. Phys.: Cond. Matter* **24**, 095003 (2012).
43. K. M. H. Young, B. M. Klahr, O. Zandi and T. W. Hamann, "Photocatalytic water oxidation with hematite electrodes," *Catal. Sci. Technol.* **3**, 1660 (2013).
44. C. Ophus, M. K. Santala, M. Asta and V. Radmilovic, "Structure and phase transitions at the interface between α-Al_2O_3 and Pt," *J. Phys.: Cond. Matter* **25**, 232202 (2013).
45. S. Cao, M. Street, J. Wang, J. Wang, X. Zhang, C. Binek and P. A. Dowben, "Magnetization at the interface of Cr_2O_3 and paramagnets with large stoner susceptibility," *J. Phys.: Condens. Matter* **29**, 10LT01 (2017).
46. K. D. Belashchenko, "Equilibrium Magnetization at the Boundary of a Magnetoelectric Antiferromagnet," *Phys. Rev. Lett.* **105**, 147204 (2010).
47. N. Wu, X. He, A. L. Wysocki, U. Lanke, T. Komesu, K. D. Belashchenko, C. Binek and P. A. Dowben, "Imaging and Control of Surface Magnetization Domains in a Magnetoelectric Antiferromagnet," *Phys. Rev. Lett.* **106**, 087202 (2011).
48. S. Cao, X. Zhang, N. Wu, A. T. N'Diaye, G. Chen, A. K. Schmid, X. M. Chen, W. Echtenkamp, A. Enders, C. Binek and P. A. Dowben, "Spin polarization asymmetry at the surface of chromia," *New J. Phys.* **16**, 073021 (2014).
49. F. Y. Yang and P. C. Hammel, "Topical review: FMR-Driven Spin Pumping in $Y_3Fe_5O_{12}$-Based Structures," *J. Phys. D: Appl. Phys.* **51**, 253001 (2018).
50. A. J. Hauser, R. E. A. Williams, R. A. Ricciardo, A. Genc, M. Dixit, J. M. Lucy, P. M. Woodward, H. L. Fraser and F. Y. Yang, "Unlocking the potential of half-metallic Sr_2FeMoO_6 films through controlled stoichiometry and double-perovskite ordering," *Phys. Rev. B* **83**, 014407 (2011).
51. B. Peters, A. Alfonsov, C. G. F. Blum, S. J. Hageman, P. M. Woodward, S. Wurmehl, B. Büchner and F. Y. Yang, "Epitaxial films of Heusler compound $Co_2FeAl_{0.5}Si_{0.5}$ with high crystalline quality grown by off-axis sputtering," *Appl. Phys. Lett.* **103**, 162404 (2013).

52. N. Nagaosa, J. Sinova, S. Onoda, A. H. MacDonald and N. P. Ong, "Anomalous Hall effect," *Rev. Mod. Phys.* **82**, 1539 (2010).
53. W. Amamou, I. V. Pinchuk, A. H. Trout, R. E. A. Williams, N. Antolin, A. Goad, D. J. O'Hara, A. S. Ahmed, W. Windl, D. W. McComb and R. K. Kawakami, "Magnetic proximity effect in Pt/$CoFe_2O_4$ bilayers," *Phys. Rev. Mater.* **2**, 011401 (2018).
54. X. Zhou, L. Ma, Z. Shi, W. J. Fan, J.-G. Zheng, R. F. L. Evans and S. M. Zhou, "Magnetotransport in metal/insulating-ferromagnet heterostructures: Spin Hall magnetoresistance or magnetic proximity effect," *Phys. Rev. B* **92**, 060402 (2015).
55. X. Liang, G. Y. Shi, L. J. Deng, F. Huang, J. Qin, T. T. Tang, C. T. Wang, B. Peng, C. Song and L. Bi, "Magnetic Proximity Effect and Anomalous Hall Effect in Pt/$Y_3Fe_{5-x}Al_xO_{12}$ Heterostructures," *Phys. Rev. Appl.* **10**, 024051 (2018).
56. T. Shang, Q. F. Zhan, H. L. Yang, Z. H. Zuo, Y. L. Xie, L. P. Liu, S. L. Zhang, Y. Zhang, H. H. Li, B. M. Wang, Y. H. Wu, S. Zhang and R.-W. Li, "Effect of NiO inserted layer on spin-Hall magnetoresistance in Pt/NiO/YIG heterostructures," *Appl. Phys. Lett.* **109**, 032410 (2016).
57. D. Z. Hou, Z. Y. Qiu, J. Barker, K. Sato, K. Yamamoto, S. Vélez, J. M. Gomez-Perez, L. E. Hueso, F. Casanova and E. Saitoh, "Tunable Sign Change of Spin Hall Magnetoresistance in Pt/NiO/YIG Structures," *Phys. Rev. Lett.* **118**, 147202 (2017).
58. W. W. Lin and C. L. Chien, "Electrical Detection of Spin Backflow from an Antiferromagnetic Insulator/$Y_3Fe_5O_{12}$ Interface," *Phys. Rev. Lett.* **118**, 067202 (2017).
59. R. Lebrun, A. Ross, S. A. Bender, A. Qaiumzadeh, L. Baldrati, J. Cramer, A. Brataas, R. A. Duine and M. Kläui, "Tunable long-distance spin transport in a crystalline antiferromagnetic iron oxide," *Nature* **561**, 222 (2018).
60. Y. T. Chen, S. Takahashi, H. Nakayama, M. Althammer, S. T. B. Goennenwein, E. Saitoh and G. E. W. Bauer, "Theory of spin Hall magnetoresistance," *Phys. Rev. B* **87**, 144411 (2013).
61. H. L. Wang, C. H. Du, P. C. Hammel and F. Y. Yang, "Comparative determination of $Y_3Fe_5O_{12}$/Pt interfacial spin mixing conductance by spin-Hall magnetoresistance and spin pumping," *Appl. Phys. Lett.* **110**, 062402 (2017).
62. W. Zhang, V. Vlaminck, J. E. Pearson, R. Divan, S. D. Bader and A. Hoffmann, "Determination of the Pt spin diffusion length by spin-pumping and spin Hall effect," *Appl. Phys. Lett.* **103**, 242414 (2013).
63. Y. Ji, J. Miao, K. K. Meng, Z. Y. Ren, B. W. Dong, X. G. Xu, Y. Wu and Y. Jiang, "Spin Hall magnetoresistance in an antiferromagnetic magnetoelectric Cr_2O_3/heavy-metal W heterostructure," *Appl. Phys. Lett.* **110**, 262401 (2017).
64. J. H. Han, C. Song, F. Li, Y. Y. Wang, G. Y. Wang, Q. H. Yang and F. Pan, "Antiferromagnet-controlled spin current transport in $SrMnO_3$/Pt hybrids," *Phys. Rev. B* **90**, 144431 (2014).
65. F. Bødker, M. F. Hansen, C. B. Koch, K. Lefmann and S. Mørup, "Magnetic properties of hematite nanoparticles," *Phys. Rev. B* **61**, 6826 (2000).
66. Y. Cheng, R. Zarzuela, J. T. Brangham, A. J. Lee, S. White, P. C. Hammel, Y. Tserkovnyak and F. Y. Yang, "Nonsinusoidal angular dependence of FMR-driven spin current across an antiferromagnet in $Y_3Fe_5O_{12}$/NiO/Pt trilayers," *Phys. Rev. B* **99**, 060405 (2019).
67. J. Fischer, O. Gomonay, R. Schlitz, K. Ganzhorn, N. Vlietstra, M. Althammer, H. Huebl, M. Opel, R. Gross, S. T. B. Goennenwein and S. Geprägs, "Spin Hall magnetoresistance in antiferromagnet/heavy-metal heterostructures," *Phys. Rev. B* **97**, 014417 (2018).

68. X. He, Y. Wang, N. Wu, A. N. Caruso, E. Vescovo, K. D. Belashchenko, P. A. Dowben and C. Binek, "Robust isothermal electric control of exchange bias at room temperature," *Nat. Mater.* **9**, 579 (2010).

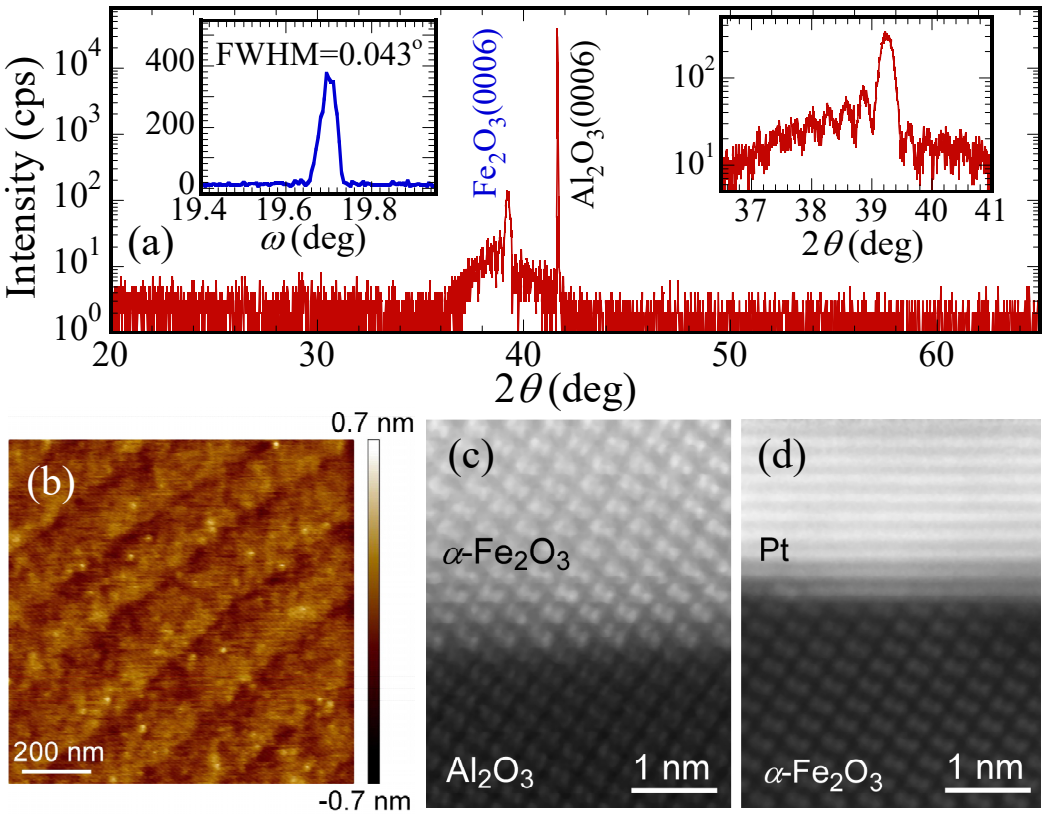
Intensity (cps)
10^4
10^3
10^2
10^1
10^0
20
30
40
50
60
2θ (deg)
(a)
FWHM=0.043°
400
200
0
19.4
19.6
19.8
ω (deg)
Fe_2O_3(0006)
Al_2O_3(0006)
10^2
10^1
37
38
39
40
41
2θ (deg)
(b)
0.7 nm
-0.7 nm
200 nm
(c)
α-Fe_2O_3
Al_2O_3
1 nm
(d)
Pt
α-Fe_2O_3
1 nm

Figure 1.

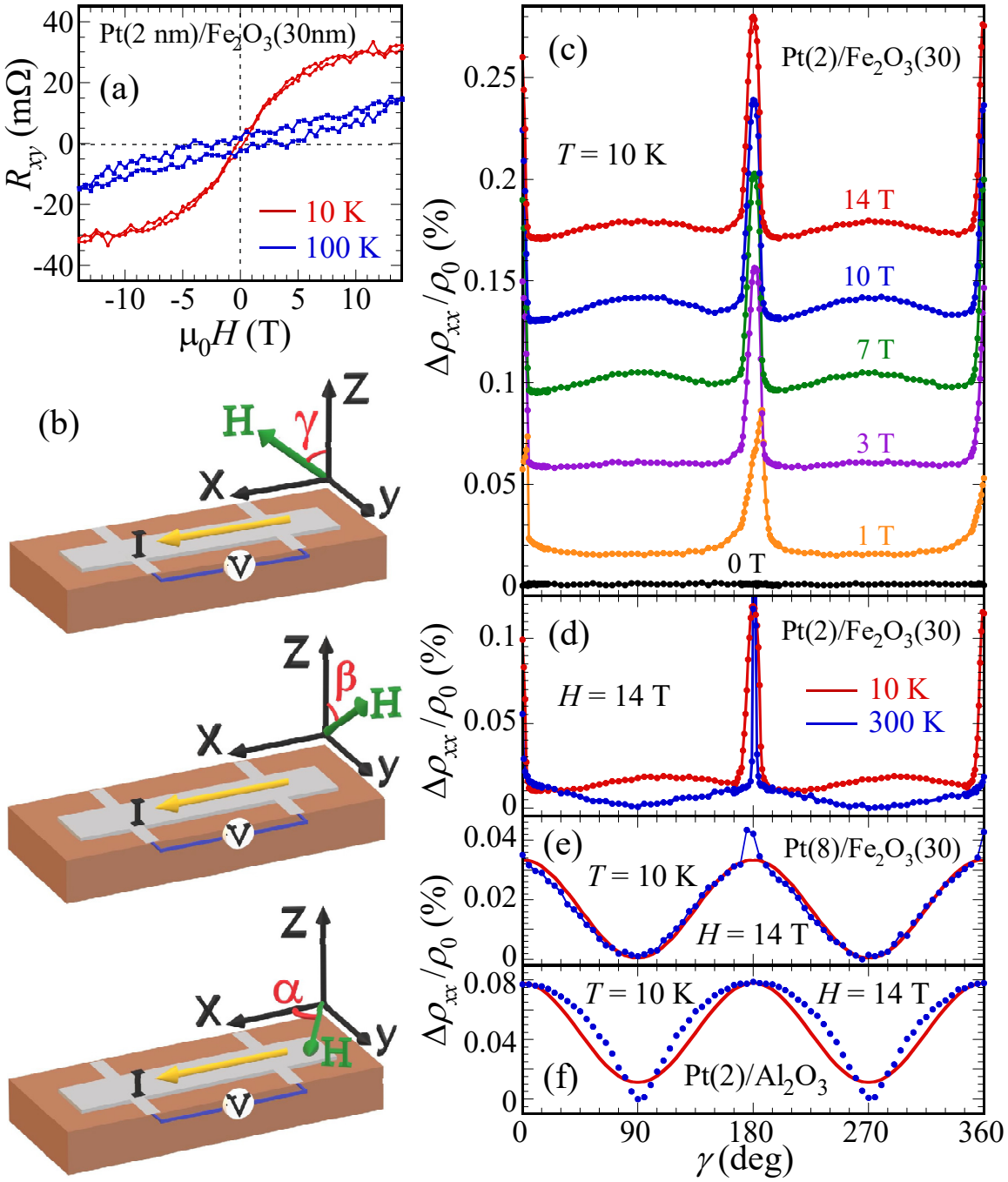
Pt(2 nm)/Fe2O3(30nm)
(a)
Rxy (mΩ)
μ0H (T)
10 K
100 K
(b)
H
γ
Z
X
y
I
V
β
α
(c)
Pt(2)/Fe2O3(30)
T = 10 K
14 T
10 T
7 T
3 T
1 T
0 T
Δρxx/ρ0 (%)
(d)
H = 14 T
10 K
300 K
(e)
Pt(8)/Fe2O3(30)
(f)
Pt(2)/Al2O3
γ (deg)

Figure 2.

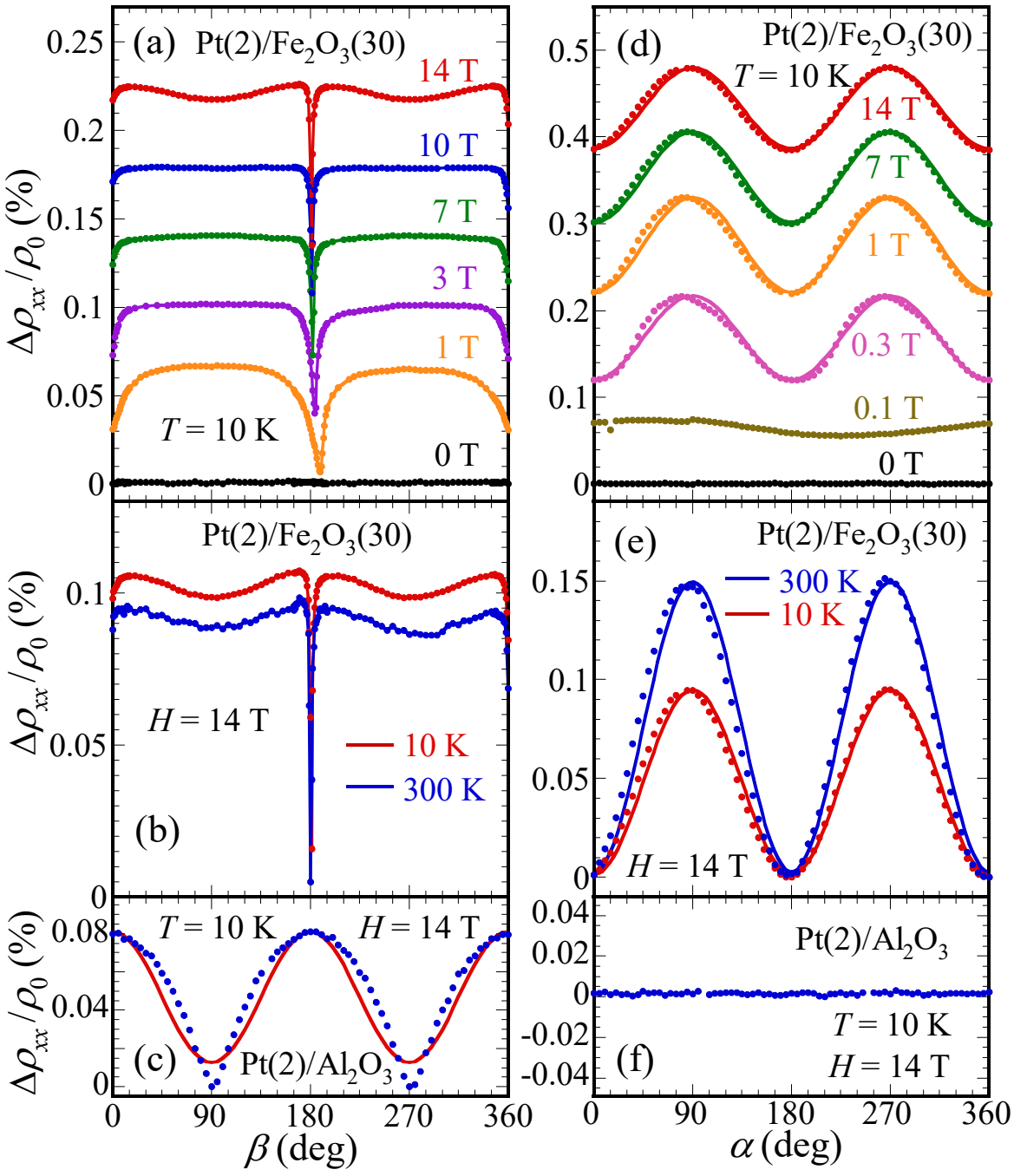
(a) Pt(2)/Fe2O3(30)
14 T
10 T
7 T
3 T
1 T
0 T
T = 10 K
Δρxx/ρ0 (%)
(b)
Pt(2)/Fe2O3(30)
H = 14 T
10 K
300 K
(c)
T = 10 K
H = 14 T
Pt(2)/Al2O3
β (deg)
(d)
Pt(2)/Fe2O3(30)
T = 10 K
14 T
7 T
1 T
0.3 T
0.1 T
0 T
(e)
Pt(2)/Fe2O3(30)
300 K
10 K
H = 14 T
(f)
Pt(2)/Al2O3
T = 10 K
H = 14 T
α (deg)

Figure 3.

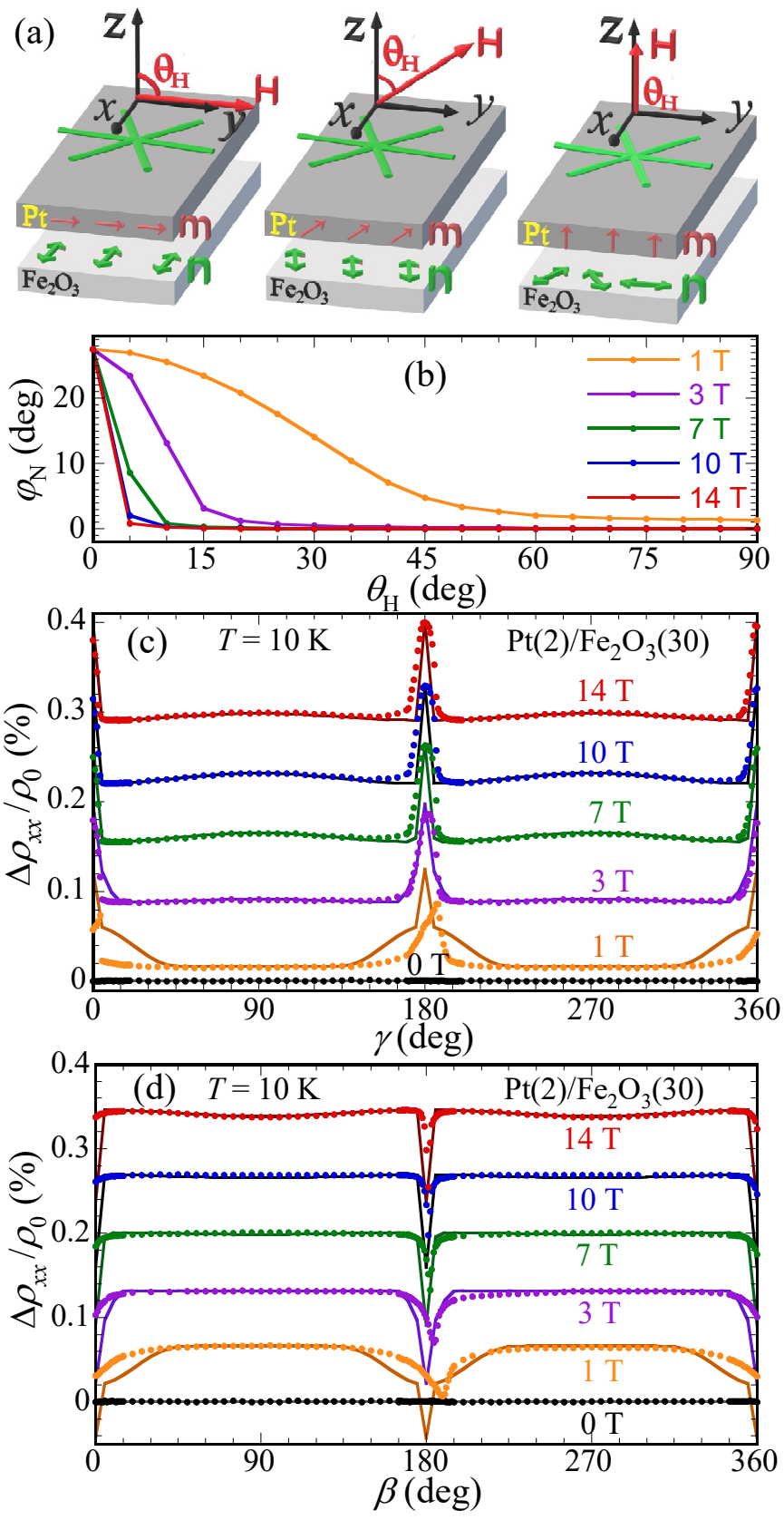
(a)
z
H
θH
x
y
Pt
m
n
Fe2O3
(b)
1 T
3 T
7 T
10 T
14 T
φN (deg)
θH (deg)
(c)
T = 10 K
Pt(2)/Fe2O3(30)
14 T
10 T
7 T
3 T
1 T
0 T
Δρxx/ρ0 (%)
γ (deg)
(d)
T = 10 K
Pt(2)/Fe2O3(30)
14 T
10 T
7 T
3 T
1 T
0 T
Δρxx/ρ0 (%)
β (deg)

Figure 4.

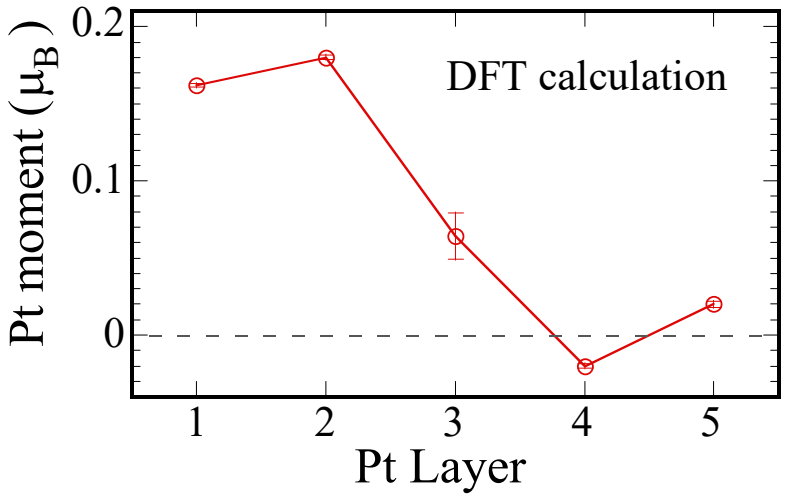

Figure 5.